Melamine sponge loading improves the separation performance of magnetic hydroxyapatite for Pb(II) adsorption

Ruifeng Li[a], Guihong Lan[a,]*, Yongqiang Liu[b], Haiyan Qiu[a], Xianfeng Ding[c], Bo Xu[a], Chunping Deng[a]

[a] *College of Chemistry and Chemical Engineering, Southwest Petroleum University (SWPU), Chengdu, 610500, China*
[b] *Faculty of Engineering and Physical Sciences, University of Southampton, Southampton SO17 1BJ, UK*
[c] *School of Sciences, Southwest Petroleum University (SWPU), Chengdu, 610500, China*

* Corresponding author
Email address: guihonglan416@sina.com (Guihong Lan)

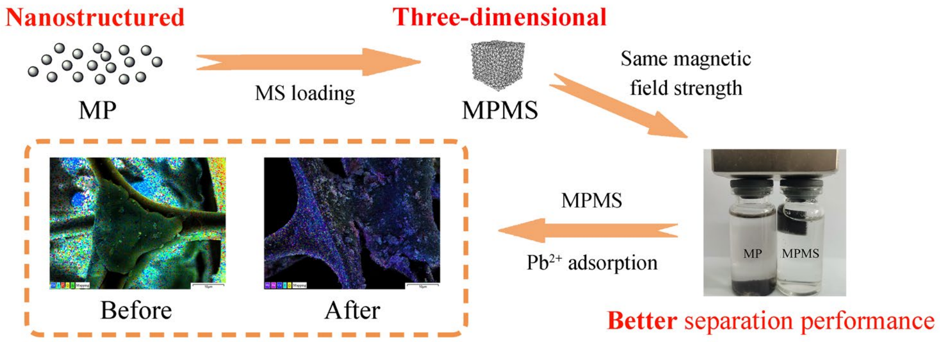

GRAPHICAL ABSTRACT

Abstract

Magnetic materials as adsorbents for wastewater treatment have attracted considerable attention because of the ease of separation of adsorbents for reuse. However, the efficient separation of magnetic materials, particularly nanoscale materials, remains challenging. Therefore, in this study, we developed an innovative method to enhance the separation performance of magnetic hydroxyapatite (MP) using melamine sponge (MS) loading. It was found that, although the magnetic moments of MP decreased from 15.54 emu/g to 11.51 emu/g after MS loading, MS-loaded MP (MPMS) exhibited better magnetic separation performance than MP. The analysis of adsorption isotherms suggests that the theoretical maximum adsorption capacity of Pb^{2+} at an initial pH of 4.85 using MPMS was 139.28 mg/g. Combined with adsorption kinetics and thermodynamics analysis, adsorption was categorized as a chemical, heterogeneous, and endothermic process. Moreover, in the adsorption mechanism, cation exchange, electrostatic interaction, dissolution/precipitation, and surface complexation mechanisms contributed 70.96%, 4.39%, 6.10%, and 18.55%, respectively, to the total Pb^{2+} removal under the experimental conditions. Hence, we provide a quick and low-cost solution for enhancing the downstream separation of magnetic adsorbents for reuse.

Keywords: Separation performance; magnetic adsorption; melamine sponge; hydroxyapatite; heavy metal

1. Introduction

Approximately 240 Pb mines have been mined worldwide, many of which have been abandoned in recent decades after mining depletion [1]. Pb^{2+} released from these abandoned mines to the environment by leaching poses severe environmental hazards and public health concerns [2] because of the non-degradability and eco-toxicity of Pb [3]. Hence, the removal of Pb from wastewater is essential. Different technologies can be used to control Pb in Pb-contaminated wastewater including adsorption [4], membrane separation [5], catalysis [6], and co-precipitation [7]. Owing to the recyclability of Pb^{2+}, it appears that adsorption-based magnetic separation for Pb^{2+} removal is more promising in the context of a circular economy for environmental protection and resource recycling [8]. The magnetic materials after Pb^{2+} adsorption can be rapidly screened from wastewater by employing an external magnetic field, thus recycling both magnetic materials and Pb [9].

To minimize the energy consumption for magnetic material recovery, the preparation of magnetic materials can be optimized to facilitate downstream separation [10, 11]. For example, preparing magnetic materials using the sol-gel method [12] can enhance the crystallinity of magnetic materials and thus achieving saturated magnetism, resulting in high-efficiency downstream separation with low energy consumption. However, the preparation conditions used in the sol-gel method are very strict, leading to high costs and low practicality [12]. For magnetic material preparation, Fe_3O_4 is generally selected as the functional chemical. Doping Co and Mn into Fe_3O_4 were found to improve the separation performance of magnetic material [13]. However, as heavy metals, Co and Mn have definite environmental risks, which restrict their practical application to enhance magnetic material separation [14]. Hence, improving the separation performance of magnetic materials is still a challenging task.

When magnetic materials are used for adsorption, magnetic crumbs are used to enhance the specific surface area for better contaminant adsorption. Thus, the downstream separation of magnetic crumbs determines the efficiency of magnetic material separation [15]. The separation performance of a magnetic crumb is poorer than that of a magnetic block with the same mass under the same external magnetic field. Therefore, an increase in the density of magnetic materials per unit volume can improve the separation performance of magnetic materials. Thus, if a method to increase the density of magnetic materials, particularly in the form of crumbs, can be established without compromising their specific surface area for contaminant adsorption, the downstream separation efficiency can be improved to reduce energy consumption.

Therefore, in this study, we aimed to develop a method to increase the density of magnetic materials by modifying a melamine sponge with magnetic hydroxyapatite (MPMS) for Pb^{2+} removal. We developed a new magnetic material with hydroxyapatite (HAP) as an effective chemical for Pb^{2+} adsorption, Fe_3O_4 as the functional chemical for magnetic separation, and melamine sponge (MS) as a carrier to increase the density of magnetic materials [16-18]. This study addresses four scientific questions: (1) the impact of bulk density on the separation performance of magnetic materials, (2) the effect of MS on the physicochemical properties of magnetic hydroxyapatite (MP), (3) the adsorption performance of Pb^{2+} using MPMS, and (4) the Pb^{2+} adsorption mechanism.

2. Materials and methods

2.1. Chemicals

Tris-HCl was purchased from Tengzhun Biotechnology Co., Ltd. (Shanghai, China); MS was purchased from Baotai Nano Material Co., Ltd. (Zhengzhou, China); $FeCl_3$, $CaCl_2$, and other chemicals were purchased from Kelong Chemical (Chengdu, China). All the chemicals used were of analytical grade, and the solutions were prepared with deionized water.

2.2. Preparation of MP and MPMS

The preparation processes for MP and MPMS are shown in **Figure 1**, and the details are provided in the supplementary material.

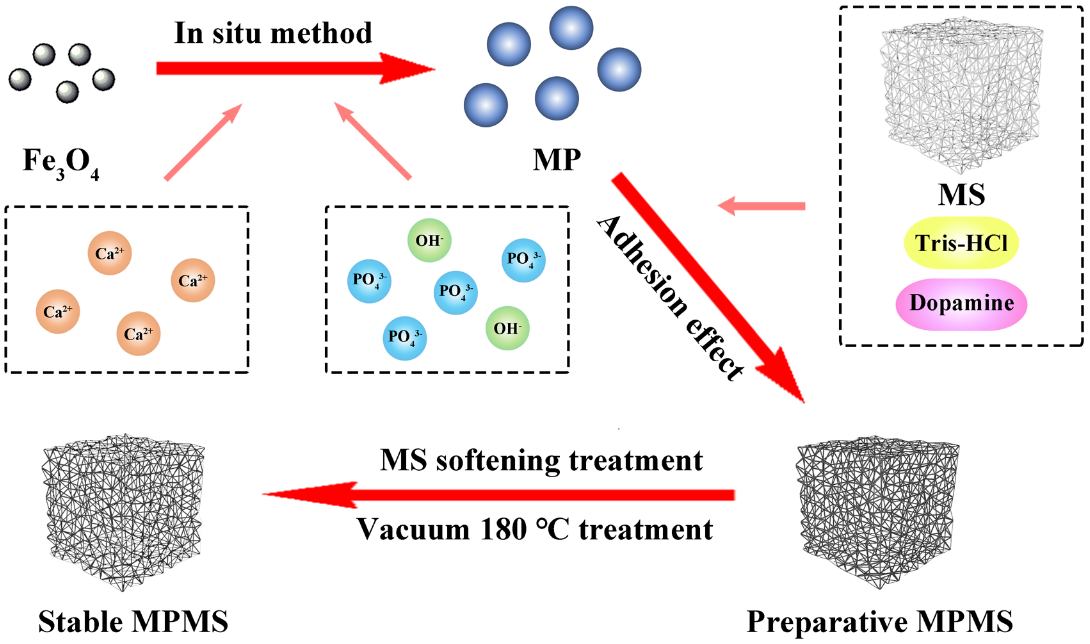

Figure 1. Preparation process diagram of magnetic hydroxyapatite (MP) and melamine sponge with magnetic hydroxyapatite (MPMS).

2.3. Characterization of MP and MPMS

The morphology was observed using scanning electron microscopy (JSM7500F, JEOL, Japan). The elemental composition was studied by energy dispersive X-ray spectroscopy (EDS, X-Max 50, Oxford Instruments, UK) and X-ray photoelectron spectroscopy (XPS, EscaLab 250XI, Thermo Scientific, USA). The chemical properties were studied using Fourier transform infrared spectroscopy (FTIR, Tensor 27, Bruker, Germany) and X-ray powder diffraction (XRD, X'Pert PRO, PANalytical Netherlands).

Other characterizations were performed by thermogravimetric analysis (TGA, SDTA851E, METTLER, Switzerland), Brunauer-Elmet-Teller (BET, ASAP2460, Micromeritics, US) method, and vibrating sample magnetometry (VSM, PPMS-0, Quantum Design, US).

2.4. Experiments

2.4.1. Study on separation performance of magnetic materials

MP and MPMS (0.4 g) were placed respectively in a vial with 45 mm height and 22 mm in diameter, containing 10 mL deionized water. To compare the separation effects of MP and MPMS, the same 1000 Gs magnetic induction intensity was applied above the vial. The effect of the MS load on MP separation performance is discussed.

2.4.2. Study on adsorption performance of magnetic materials

For the basic adsorption experiments, the following conditions were set: pH as 4.85, without adjustment, 0.080 g adsorbent dosage to 50 mL Pb^{2+} solution, 3 h adsorption time, 300 mg/L Pb^{2+} concentration, and 25 °C temperature. With single-factor optimization experiments, the effects of pH (4-7), MPMS dosage (0.040-0.200 g), time (5-2160 min), initial Pb^{2+} concentration (200-400 mg/L), and temperature (5-45 °C) on the adsorption of Pb^{2+} using MPMS were studied. The Pb^{2+} concentration in the solution was quantified using an atomic absorption spectrophotometer (SP-3520AA, Spectrum Instruments, China).

Five cations (Na^+, K^+, Ca^{2+}, Mg^{2+}, and Fe^{3+}) at 0.05 M concentrations were selected to interfere with the adsorption of Pb^{2+} by MPMS. HNO_3-5 (pH = 5), 0.1 M $Ca(NO_3)_2$, 0.1 M NaOH, and saturated $Ca(OH)_2$ were selected as eluents to desorb the adsorbed Pb^{2+} by MPMS for the reuse of MPMS in the following cycle. $Ca(OH)_2$ was found with the best elution effect and was thus selected for adsorption-desorption experiments for five consecutive cycles.

2.4.3. Study on adsorption process of magnetic materials

The adsorption process of Pb^{2+} by MPMS was studied by adsorption kinetic, isothermal, and thermodynamic models. Specifically, the adsorption kinetic model was fitted with pseudo-first-order, pseudo-second-order, and intraparticle diffusion kinetic models. The adsorption isotherm model was fitted using the Langmuir, Freundlich, Temkin, and D-R models. The adsorption thermodynamic model was fitted using the van't Hoff equation.

2.4.4. Study on adsorption mechanisms

In this study, 0.05 M Na^+ was used as the main interfering cation to judge competitive electrostatic interactions between the cations and MPMS. Furthermore, the ion exchange of Ca^{2+} in MPMS with Pb^{2+} in the solution was evaluated using a blank group.

2.5. Calculation

The load factor of MP in MPMS was calculated as follows [19]:

$$\eta_1 = \frac{m_b - m_a}{m_a} \tag{1}$$

where m_b and m_a are the mass of MS and MPMS (g).

The adsorption capacity of Pb^{2+} by MPMS was calculated as follows [20]:

$$q_e = \frac{(C_o - C_e) \times V}{m} \tag{2}$$

where C_0 and C_e are the initial and equilibrium Pb^{2+} concentrations in the solution (mg/L), respectively, V is the volume of the experimental solution (L), m is the mass of the MPMS (g).

The contribution rate of Ca^{2+} exchange with Pb^{2+} to the overall adsorption of Pb^{2+} by MPMS was calculated using the following formulas [21]:

$$Ca_E = nCa_R^{2+} - nCa_B^{2+} = \frac{C_E \cdot V}{M} - \frac{C_B \cdot V}{M} \tag{3}$$

$$\eta_2 = \frac{Ca_E \cdot M_{Pb}}{m_e} \cdot 100\% \tag{4}$$

where Ca_E is the number of moles of Ca^{2+} for the ion-exchange mechanism (mol), nCa_R^{2+} and nCa_B^{2+} are the moles of Ca^{2+} in the solutions of the adsorption experiment with Pb^{2+} and the blank group (mol) without Pb^{2+}, respectively, and C_E and C_B are the concentrations of Ca^{2+} in the adsorption experimental and blank groups (g/L), respectively, V is the volume of the solution (L) and M and M_{Pb} are the atomic weights of Ca and Pb (g/mol), respectively, and m_e is the total mass of Pb^{2+} adsorbed by MPMS in solution (g).

This study performed three replicate experiments. Experimental results were represented by mean values and processed using OriginPro 2016.

3. Results

3.1. Study on the separation performance of MS and MPMS

The magnetic moment is often employed as the dominating indicator of the separation performance of magnetic materials. **Figure 2** shows the magnetism of 0.4 g MP and MPMS, under the same range of magnetic fields from -20000 Oe to 20000 Oe. After loading MS, the magnetic moment of MP decreased from 15.54 emu/g to 11.51 emu/g due to less MP per unit of MPMS. However, as shown in **Figure 2**, under the same magnetic field conditions, MPMS showed better separation performance than MP because of the movement of the whole block of material instead of individual crumbs.

Further, after five consecutive adsorption-desorption cycles, MPMS still maintained a magnetic moment of 8.80 emu/g, indicating that MPMS still exhibits acceptable magnetism even after being used five times.

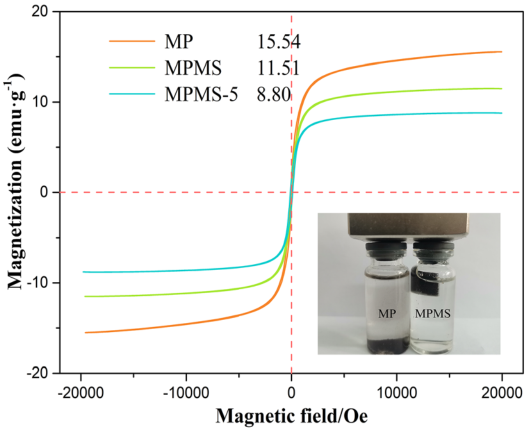

Figure 2. Magnetism of MP and MPMS within a range of magnetic field strengths.

3.2. Study on the Pb^{2+} adsorption using MPMS

Because MPMS demonstrated better magnetic separation performance, MPMS was further investigated for Pb^{2+} adsorption under different conditions.

3.2.1. pH effects on Pb^{2+} adsorption using MPMS

As shown in **Figure 3a**, with the pH raised, the adsorption capacity of Pb^{2+} by MPMS increased linearly and reached 136.07 mg/g at a pH of 5.5. Subsequently, with the further increase in pH above 5.5, the adsorption capacity of Pb^{2+} by MPMS decreased linearly but more steeply. The adsorption capacity of Pb^{2+} was only 117.66 mg/g at a pH of 7.0. When the pH exceeded 5.5, white $Pb(OH)_2$ precipitated in the solution, and the Pb^{2+} concentration decreased. The $Pb(OH)_2$ precipitates blocked the pores of MPMS and thus reduced the active surface area of MPMS for Pb^{2+} adsorption. Moreover, the pH value of the solution showed varying levels of increase after adsorption, indicating that chemical reactions occurred during the adsorption.

In addition, the Ca^{2+} concentration in the solution decreased with increasing pH. This is mainly because HAP has a higher solubility at lower pH, resulting in Ca^{2+} release from HAP in MPMS into the solution. Although the pH affects the Pb^{2+} adsorption capacity, it was found that the Pb^{2+} adsorption capacity changed by 13.53% when the pH varied from 4 to 7. Thus, the pH in the subsequent experiments was not adjusted, i.e., 4.85. At this time, the pH value of the solution after adsorption was 5.43, which did not reach the threshold of $Pb(OH)_2$.

3.2.2. Dosage of MPMS on Pb^{2+} adsorption

MPMS can provide adsorption sites. The adsorption capacity of Pb^{2+} by MPMS decreased with an increase in dosage, whereas the removal rate reached a stable value of 95.20% when the dosage exceeded 120 mg (**Figure 3b**). This is because an increase in the dosage of MPMS reduced the actual adsorption per unit MPMS for a constant Pb^{2+} amount [22]. Based on the removal rate of Pb^{2+} in 300 mg/L Pb^{2+} solution in this experiment, it is recommended to select dosage of 120 mg MPMS corresponding to a 2.4 g/L MPMS dosage in practice. However, to better analyze the adsorption process and adsorption mechanism, an 80 mg dosage of MPMS that could not fully adsorb 300 mg/L Pb^{2+} was chosen for subsequent experiments.

3.2.3. Effects of interfering cations on Pb^{2+} adsorption by MPMS

Figure 3f shows that (1) monovalent cations (Na^+ and K^+) exerted the least influence on the adsorption of Pb^{2+} by MPMS. When the concentration of Na^+ and K^+ was 0.05 M, the adsorption of Pb^{2+} by MPMS was 95.61% and 90.87%, respectively, of that without interfering cations. (2) The effect of divalent cations (Ca^{2+} and Mg^{2+}) on the adsorption of Pb^{2+} by MPMS was greater than that of the monovalent cations. The influence of Ca^{2+} was significantly greater than that of Mg^{2+}. The adsorption capacity was reduced by 46.98% in the presence of 0.05 M Ca^{2+} and by 24.69% in 0.05 M Mg^{2+}. (3) The trivalent cation (Fe^{3+}) had the greatest negative influence on the adsorption of Pb^{2+} by MPMS. Its adsorption capacity was reduced to 44.51% of that without interfering cations.

Previous studies on Pb^{2+} adsorption [18] reported that Na^+, K^+, and Mg^{2+} mainly inhibit adsorption by electrostatic repulsion. Ca^{2+} mainly inhibits adsorption through the common ion effect, and Fe^{3+} mainly affects adsorption by competitive adsorption. The negative interference of the five cations on the adsorption of Pb^{2+} by MPMS was in the following order: $Fe^{3+} > Ca^{2+} > Mg^{2+} > K^{+} > Na^{+}$.

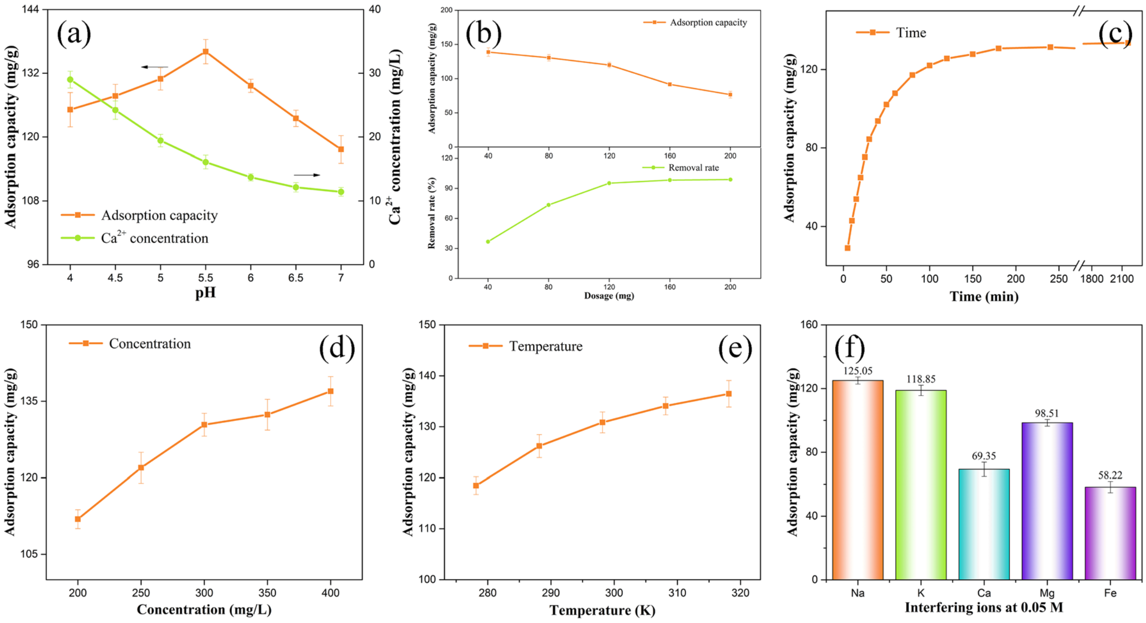

Figure 3. Adsorption performance of Pb^{2+} by MPMS. (**a**, **b**, **c**, **d**, **e**, and **f** show the adsorption capacity of Pb^{2+} by MPMS under different pH, MPMS dosage, adsorption time, Pb^{2+} concentration, adsorption temperature, and different interfering cations, respectively).

3.2.4. Pb^{2+} adsorption by regenerated MPMS

As shown in Figure S1, among different eluents, $Ca(OH)_2$ demonstrated the best Pb^{2+} adsorption capacity by regenerated MPMS. It showed an adsorption capacity of 67.85 mg/g with 48.13% reduction. Furthermore, after five regeneration cycles and reuse, MPMS still showed an adsorption capacity of 56.04 mg/g and tended to be stable.

3.3. Study on adsorption process

3.3.1. Adsorption kinetics

In the kinetic model, if the range of the fitting interval exceeds the equilibrium time, the accuracy of the fitting is negatively affected [23]. Hence, the fitting intervals of the pseudo-first-order and pseudo-second-order kinetic models were set to 5-180 min and that of the intra-particle diffusion kinetic model was set to 5-2160 min. The kinetic formulas for pseudo-first-order kinetics, pseudo-second-order kinetics, and intra-particle diffusion kinetics are shown in Equations 5, 6, and 7, respectively [24]:

$$log(q_e - q_t) = log(q_e) - \frac{k_1}{2.303}t \tag{5}$$

$$\frac{t}{q_t} = \frac{1}{k_2 q_e^2} + \frac{t}{q_e} \tag{6}$$

$$q_t = k_i t^{0.5} + C \tag{7}$$

where t is the experimental time (min), q_e and q_t represent the adsorption capacity at equilibrium and at time t (mg/g), respectively, k_1 is the pseudo-first-order constant (min^{-1}), k_2 is the pseudo-second-order constant (g·mg^{-1}·min^{-1}), k_i is the intra-particle diffusion kinetic constant, and C is a constant related to the thickness of the boundary layer.

As shown in Figure S2 and **Table 1**, the pseudo-second-order kinetic model (R^2 = 0.9990) provided a better fit than the pseudo-first-order kinetic model (R^2 = 0.9868). The theoretical adsorption capacity (q_e = 149.03 mg/g) of the pseudo-second-order kinetic model was also closer to the actual adsorption capacity (q_{cal} = 133.63 mg/g). Hence, based on the pseudo-second-order kinetic model, it can be hypothesized that the adsorption of Pb^{2+} by MPMS is mainly due to chemical adsorption [22].

The intraparticle diffusion model (**Table 2**) also shows an ideal fit for the adsorption process. In the initial stage (k_3 = 14.86), Pb^{2+} moved from the solution to the surface of MPMS, mainly through electrostatic interactions between Pb^{2+} and functional groups such as PO_4^{3-} and OH^- on MPMS [25]. Subsequently (k_4 = 2.92), Pb^{2+} on the surface diffused into the interior of the MPMS through the macropores and mesopores. Finally (k_5 = 0.07), Pb^{2+} was adsorbed to the MPMS through the micropores, and as the adsorption proceeded, the slopes in Figure S2c decreased gradually as the intercepts increased, indicating that as the adsorption proceeded, the resistance of the MPMS to Pb^{2+} adsorption increased [26]. Moreover, the fitting line in Figure S2c did not pass through the coordinate origin, indicating that diffusion was not the only limiting factor for the adsorption of Pb^{2+} by MPMS [27].

Table 1. Pseudo-first-order and pseudo-second-order kinetic model parameters of Pb^{2+} adsorption by MPMS.

Parameters	Pseudo-first order			Pseudo-second order		
	q_{e1} ($mg \cdot g^{-1}$)	k_1 (min^{-1})	R^2	q_{e2} ($mg \cdot g^{-1}$)	k_2 ($g \cdot mg^{-1} \cdot min^{-1}$)	R^2
MPMS	97.32	0.0202	0.9868	149.03	2.84×10^{-4}	0.9990

Table 2. Intra-particle diffusion model parameters of Pb^{2+} adsorption by MPMS.

Parameters	Intra-particle diffusion								
	5 - 60 min			80 - 180 min			210 - 4320 min		
	k_3	c_1	R^2	k_4	c_2	R^2	k_5	c_3	R^2
MPMS	14.86	-2.21	0.9849	2.92	92.26	0.9502	0.07	130.64	0.9198

3.2.2. Adsorption isothermal

The fitting interval of the initial concentration in the isothermal model was set to 200-400 mg/L, and the formulas for the Langmuir, Freundlich, Temkin, and D-R isothermal models are as follows [28, 29]:

$$\frac{c_e}{q_e} = \frac{1}{q_m K_L} + \frac{c_e}{q_m} \tag{8}$$

$$ln(q_e) = ln(K_F) + \frac{1}{n} ln(c_e) \tag{9}$$

$$B = \frac{RT}{b_T} \tag{10}$$

$$q_e = Bln(a_T) + Bln(c_e) \tag{11}$$

$$\varepsilon = RTln(1 + 1/c_e) \tag{12}$$

$$ln(q_e) = ln(q_m) - \beta\varepsilon^2 \tag{13}$$

where c_e is Pb^{2+} the concentration of the solution at equilibrium (mg/L), q_e and q_m are the adsorption capacities at the equilibrium and maximum, respectively (mg/g), K_L and K_F are the Langmuir and Freundlich constants, *1/n* denotes the intensity of the adsorption process, *B* and b_T are the Temkin constants, *R* is the universal gas constant (8.314 $J \cdot mol^{-1} \cdot K^{-1}$), *T* is the temperature (K), ε is the Polanyi potential, and β is the activity coefficient.

Among the models stated above, the Langmuir model is mainly based on two assumptions: (1) adsorption occurs on the adsorbent surface, and (2) the adsorbent surface is uniform [30]. The Freundlich model is suitable for non-ideal adsorption processes [21]. When $1/n < 1$, the adsorption reaction was considered favorable. The Temkin model is typically used to evaluate the relationship between adsorption energy and coverage [31]. The D-R model was primarily employed to evaluate the adsorption process of microporous structures [32].

Figure S3 and **Table 3** show the results of the isothermal models. It can be found that the Freundlich model ($R^2 = 0.9993$) exhibited the best fitting. Hence, the adsorption of Pb^{2+} by MPMS can be considered heterogeneous on the surface [21]. Because *1/n* in Freundlich < 1, the adsorption of Pb^{2+} by MPMS can be considered advantageous. In addition, both the Langmuir and Temkin constants show a good fit to the adsorption process. From the Langmuir model, the theoretical maximum adsorption capacity of Pb^{2+}, i.e., q_m, by MPMS was 139.28 mg/g. The b_T in the Temkin model illustrates that the binding energy between Pb^{2+} and MPMS is about 265.03 kJ/mol [31]. However, the D-R model ($R^2 = 0.7318$) for microporous structure-based materials cannot be used to explain adsorption by MPMS with a mesoporous structure.

Table 3. Adsorption isothermal model parameters of Pb^{2+} adsorption by MPMS

Isothermal Model	Parameters	MPMS
Langmuir constants	q_m ($mg \cdot g^{-1}$)	139.2758
	k_L ($L \cdot mg^{-1}$)	0.1912
	R^2	0.9990
Freundlich constants	k_F ($L \cdot mg^{-1}$)	91.9624
	1/n	0.0757
	R^2	0.9993
Temkin constants	B	9,3529
	α_T	11450.3084
	b_T	265.0330
	R^2	0.9972
D-R constants	q_m ($mg \cdot g^{-1}$)	131.2534
	β	5.1×10^{-6}
	R^2	0.7318

3.3.3. Adsorption thermodynamics

The fitting interval of the temperature in the thermodynamic model was set to 5-45 °C, and the thermodynamic parameters were calculated as follows [33]:

$$K_c = \frac{q_e}{c_e} \tag{14}$$

$$\mathit{\Delta} G^0 = -RTlnK_c \tag{15}$$

$$lnK_c = -\frac{\mathit{\Delta} H^0}{RT} + \frac{\mathit{\Delta} S^0}{R} \tag{16}$$

where K_c is the thermodynamic equilibrium constant, T is the temperature (K), q_e is the adsorption capacity at equilibrium (mg/g), c_e is Pb^{2+} concentration at equilibrium (mg/L), and R is the universal gas constant (8.314 $J \cdot mol^{-1} \cdot K^{-1}$).

As shown in **Table 4**, $\mathit{\Delta} G$ was less than 0, indicating that the adsorption process was spontaneous and thermodynamically favorable [30]. $\mathit{\Delta} G$ gradually decreased with the increase in temperature. Combining the adsorption results of MPMS at different temperatures (**Figure 3d**) and $\mathit{\Delta} H$ value (**Table 4**), it can be concluded that a higher temperature was conducive to the adsorption [33]. $\mathit{\Delta} S$ exceeds 0, indicating that the interface randomness between the adsorbent MPMS and the adsorbate Pb^{2+} decreased after adsorption [34].

Table 4. Adsorption thermodynamic model parameters of Pb^{2+} adsorption by MPMS

T(K)	ΔG (kJ mol^{-1})	ΔH (kJ mol^{-1})	ΔS (J $mol^{-1}K^{-1}$)
278.15	-0.20	9.50	35.09
288.15	-0.65		
298.15	-1.04		
308.15	-1.30		
318.15	-1.61		

3.4. Characterization of MPMS

3.4.1. Observation of morphologic structure using scanning electron microscopy

Figure S4 shows the morphologies of the MS, MP, MPMS, and MPMS-Pb (after adsorption). Comparing the morphologies of MS and MPMS, it was found that MP successfully adhered to the intersection of sponge fibers as the intersection provided more attachment sites for MP. Comparing the morphologies of MPMS and MPMS-Pb, it was found that the structure of MPMS remained stable after Pb^{2+} adsorption, which is consistent with the observation that no particulate matter peeled off during the experiment. Because MPs are nano-sized, their high specific surface area conferred by the nanostructure is conducive to the adsorption of heavy metal pollutants by MPMSs [35].

3.4.2. Elemental composition analysis by EDS, XPS

Figure 4 shows the EDS and XPS spectra of MPMS and MPMS-Pb, and the elemental compositions are summarized in Table S1. Through EDS, it can be seen that MPs were mainly located at the intersection of the sponge. Before adsorption, the surface of MPMS was mainly composed of HAP elements, that is, Ca, O, and P. After adsorption, Pb is observed at the intersection of the sponge. Thus, MP plays a dominant role in the adsorption of Pb^{2+} by MPMS.

In addition, the Ca/P ratio was approximately 1.6 in the virgin MPMS with Ca and P, mainly from HAP. The ratio of Fe_3O_4 to HAP was approximately 0.25. Hence, the combination of MS and MP did not change the Ca/P and Fe_3O_4/HAP ratios. After Pb^{2+} adsorption, the mass percentages of Ca and Fe in the MPMS decreased from 11.80% to 3.28% and 15.57% to 10.66%, respectively, while the mass percentage of Pb increased from 0.00% to 12.44%, indicating that the Ca and Fe in MPMS may be involved in the adsorption of Pb^{2+} by MPMS.

In the XPS spectrum of MPMS, C1s can be found as C-C (284.80 eV), C-N (287.54 eV), C=N (286.19 eV), and N=C-N (288.39 eV) [36]. O1s were identified as P-O (531.54 eV), P=O (532.89 eV), and Fe_3O_4 (530.84 eV) in MP [37]. N1s were identified as C-N=O (398.64 eV), N-C (399.69 eV), and -NH- (400.64 eV) [38]. The Ca2p peaks were identified as $Ca2p_{3/2A}$ (347.44 eV), $Ca2p_{1/2A}$ (350.90 eV), $Ca2p_{3/2B}$ (348.54 eV), and $Ca2p_{1/2B}$ (351.69 eV) in HAP [37]. The P2p peaks were identified as $P2p_{3/2A}$ (133.24 eV), $P2p_{1/2A}$ (133.94 eV), $P2p_{3/2B}$ (134.64 eV), and $P2p_{1/2B}$ (135.49 eV) in HAP [37]. The values of 710.94 eV, 724.74 eV, 713.84 eV, and 716.64 eV of Fe2p can be identified as Fe_3O_4 [39]. These results show that both MS and MP were present in MPMS, indicating the successful preparation of MPMS. In summary, MS, Fe_3O_4, and HAP retained their original chemical structures after loading MP into MS.

After adsorption, the characteristic peaks of Pb4f increased significantly and were identified as $Pb4f_{7/2}$ (138.95 eV), $Pb4f_{5/2}$ (143.75 eV), P-O (144.95 eV), and Pb=O (140.05 eV). Among them, $Pb4f_{7/2}$ and $Pb4f_{5/2}$ can be primarily attributed to the adsorption of Pb^{2+} by HAP, whereas the presence of Pb-O and Pb=O can be attributed to the reaction of Fe_3O_4 and Pb^{2+} [39], indicating that both HAP and Fe_3O_4 played a role in Pb^{2+} adsorption. In addition, it was found that the peaks of Ca2p and Fe2p reduced significantly, whereas that of P2p increased. Combined with the results of the VSM and subsequent XRD, it can be concluded that (1) ion exchange between Ca^{2+} from HAP and Pb^{2+} in the solution played a momentous role in the adsorption of Pb^{2+} by MPMS. Therefore, more P was exposed in the MPMS. (2) The Fe_3O_4 on the surface of the MPMS reacted with Pb^{2+} to produce a small amount of Pb_3O_4. This mechanism for Pb^{2+} removal from solution is usually neglected when magnetic materials are used as adsorbents. However, Fe_3O_4 inside the MPMS did not participate in the adsorption because neither the Fe_3O_4 diffraction peak in XRD nor the magnetic moments measured by VSM were detected, and no significant decrease was observed after adsorption.

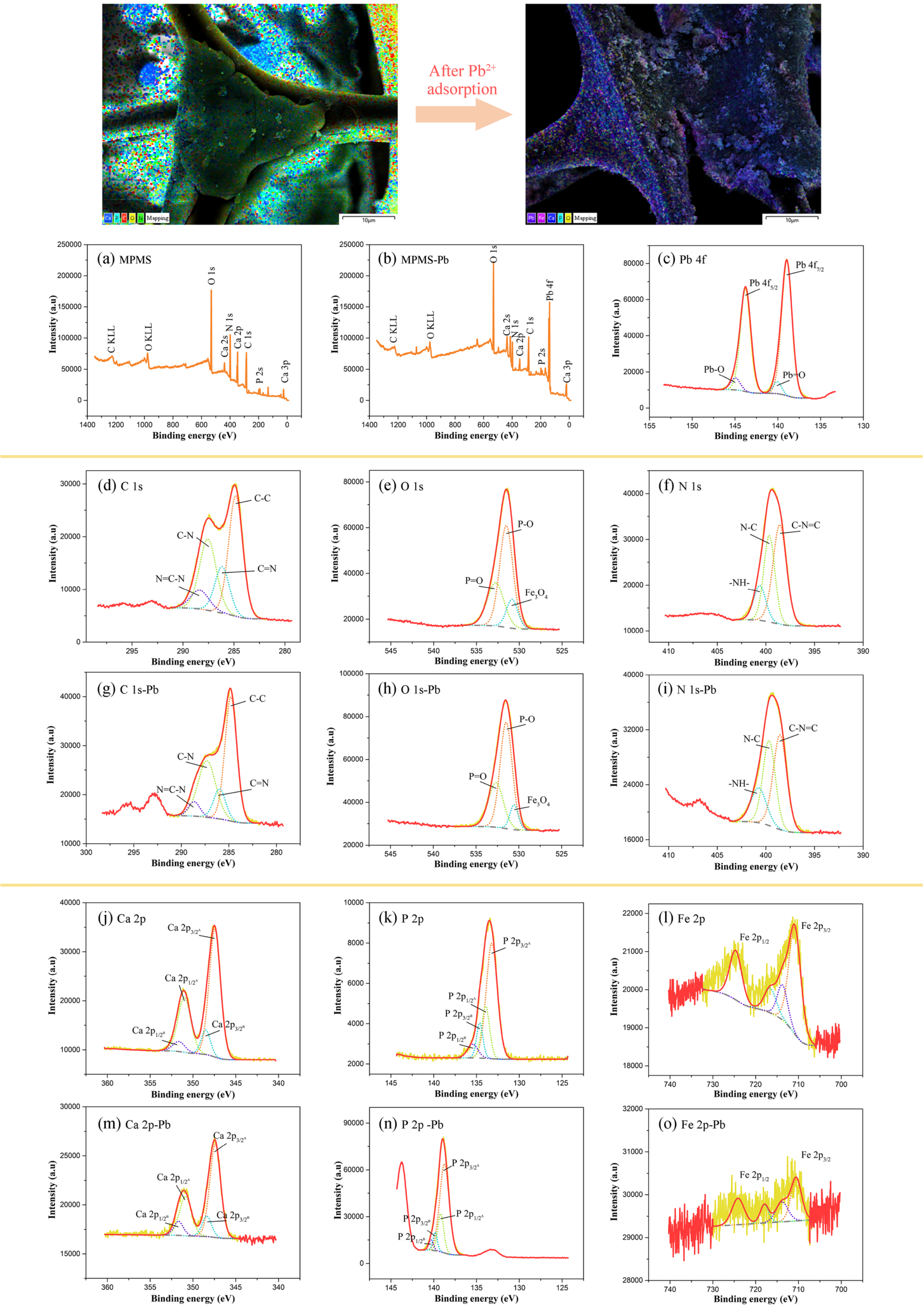

Figure 4. Energy dispersive X-ray spectroscopy (EDS) mapping and X-ray photoelectron spectroscopy (XPS) spectrum of MPMS and MPMS-Pb.

3.4.3. Chemical properties analyzed using FTIR and XRD

To evaluate the chemical properties, the functional groups of MS, MP, and MPMS were tested using FTIR in ATR mode, and the chemical components of MS, MP, MPMS, MPMS-Pb, and MPMS-Ca (after $Ca(OH)_2$ recycling) were tested using XRD. As shown in **Figure 5a**, obvious adsorption peaks were observed at 811 cm^{-1} in both MS and MPMS, which corresponded to the unique triazine ring in MS [40]. Furthermore, the broad peak at 3318 cm^{-1}, close to the -OH peak at 3400 cm^{-1}, was mainly attributed to the N-H functional group in MS. The peaks at 2924 cm^{-1}, 2852 cm^{-1}, 1556 cm^{-1}, 1343 cm^{-1}, and 1330 cm^{-1} correspond to $-CH_2-$, $-CH_2-$, C=N, C-O, and C-H in MS, respectively [40]. It is worth noting that the loading of MP caused a distinct peak at 1029 cm^{-1} in MPMS, which was caused by the vibration of Fe-O and P=O in MP [41, 42], further proving that MP was successfully loaded onto the MS, while MPMS maintained the chemical properties of both MS and MP.

The XRD results are presented in **Figure 5b**. As MS is an organic material without a crystal structure, no XRD diffraction peaks were detected. In MP and MPMS, the peaks of Fe_3O_4 at 30.10°, 35.42°, 43.05°, 53.39°, 56.94°, and 62.52° and the HAP peaks at 25.88°, 31.77°, 46.91°, 49.47°, and 53.14° were detected. While verifying the successful synthesis of MP (**Figure 5b)**, it was observed that the chemical properties of MP remained intact even after combining with MS. By comparing MPMS and MPMS-Pb, it can be observed that the peaks of HAP decreased significantly after the adsorption, while those of $Pb_{10}(PO_4)_6(OH)_2$ appeared correspondingly, suggesting that ion exchange existed in the adsorption of Pb^{2+} by MPMS. In addition, MPMS-Ca results imply that, under alkaline conditions, Ca^{2+} in the solution replaced Pb^{2+} in the environment, indicating the ideal recycling potential of MPMS [43].

3.4.4. TGA and BET analysis

From the TGA results (**Figure 5c**), it can be observed that the weight loss of MP at 800 ℃ was only 1.18%, as MP primarily comprises inorganic HAP and stable Fe_3O_4. In contrast, MS and MPMS started to show significant weight loss when the temperature exceeded 200 ℃. The weight loss of MPMS in the temperature range of 200-600 ℃ can be ascribed to the thermal degradation of MS and loss of bound water [38]. When the temperature increased to 609.5 ℃, MS was completely pyrolyzed. At 800 ℃, the weight loss of MPMS was 19.77%, which is consistent with the MS content in MPMS.

The BET results for MS, MP, and MPMS are shown in **Figure 5d**, **5e**, and Table S2. The isotherms of the three materials mentioned above are all type IV, which corresponds to the capillary phenomenon of porous materials. Owing to the doping of the narrow MP, the hysteresis loop of the MPMS changed from H3 to H4 type [41]. From the pore size distribution shown in **Figure 5e**, it can be seen that the pores were mainly mesoporous. After MP was loaded onto MS, the specific surface area increased from 4.56 m^2/g of MS to 48.23 m^2/g of MPMS. Meanwhile, the pore volume and size increased from 0.01 cm^3/g to 0.27 cm^3/g, and 11.81 nm to 22.08 nm, respectively. Therefore, the loading of MPs increased the dispersion of the internal structure of the MS.

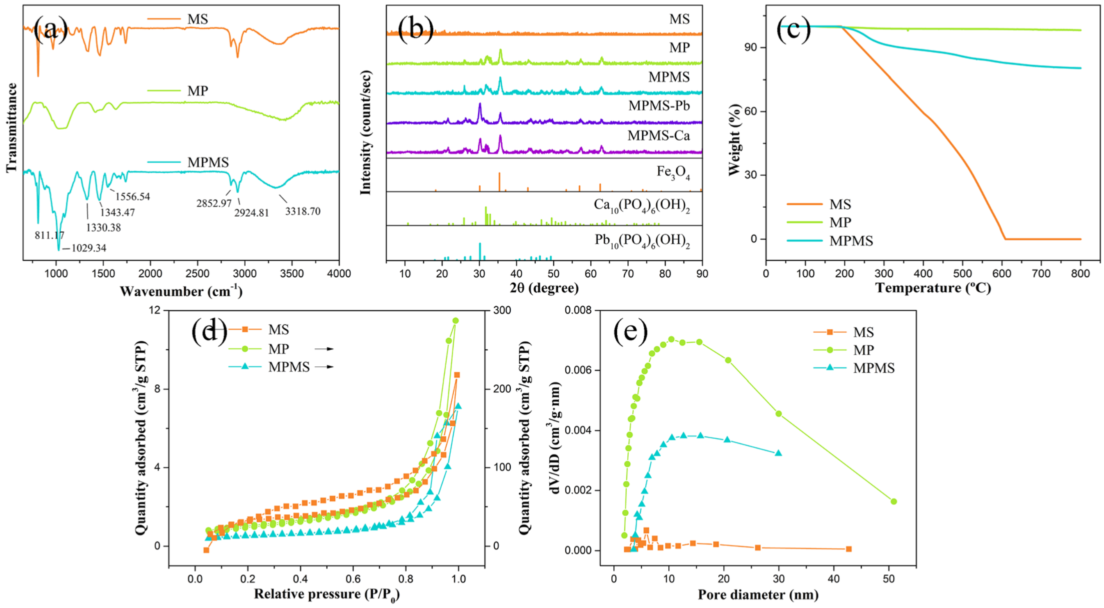

Figure 5. Characterization of MS, MP, and MPMS using Fourier transform infrared spectroscopy (FTIR), X-ray powder diffraction (XRD), thermogravimetric analysis (TGA), and Brunauer-Elmet-Teller (BET) method.

4. Discussion

4.1. Effects of MP loading to MS on magnetic separation performance

Although loading MP to MS reduced the magnetic moments of MPMS as the magnetic material per unit mass decreased, the magnetic separation of MPMS was higher than that of MP at the same magnetic field strength. Interestingly, magnetic materials exhibit diametrically opposite results in terms of their magnetic moments and magnetic separation performance.

The magnetic flux can be calculated by multiplying the intensity of magnetic induction by the density of the magnetic induction line [44]. Under the same magnetic induction intensity, MP, the magnitude of the magnetic flux is positively related to the density of the magnetic induction line, that is, the density of the magnetic material. In this study, the nanostructure increased the specific surface area, while it limited the separation performance of the magnetic material owing to the increase in dispersion. As shown in **Figure 6**, by loading a nanomagnetic material on a three-dimensional carrier such as MS, the separation performance of the magnetic material can be improved, thus reducing the operating energy consumption. It may not be suitable to express the separation performance using the magnetic moment.

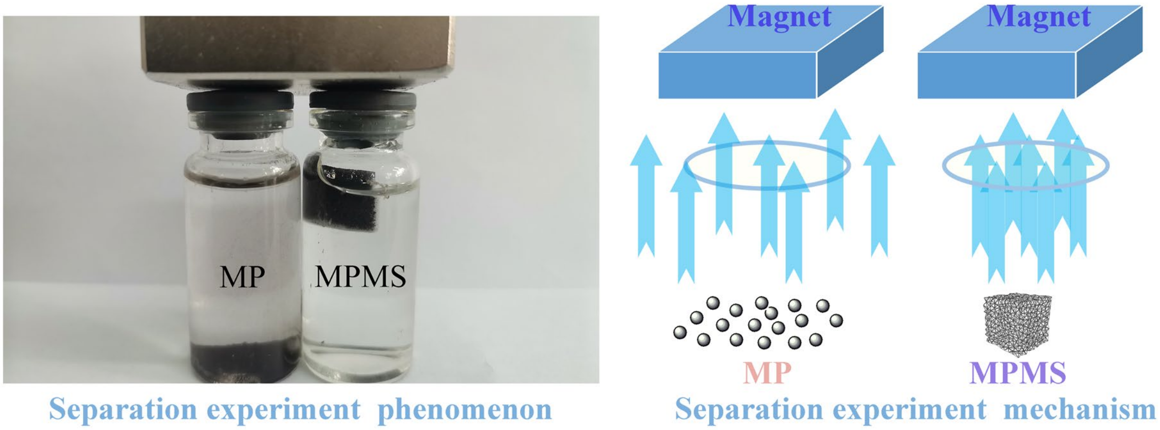

Figure 6. Comparison of magnetic separation performance of MP and MPMS at the same magnetic field strength.

4.2. Cation exchange on adsorption of Pb^{2+} by MPMS

The surface of HAP in the MPMS can provide adsorption sites. From the pseudo-second-order kinetic model, XPS, and XRD analysis, Ca^{2+} in MPMS could be exchanged with Pb^{2+} in solution, which can be expressed by the following formula [22]:

$$Ca_{10}(PO_4)_6(OH)_2 + xPb^{2+} \leftrightarrow Ca_{10\text{-}x}Pb_x(PO_4)_6(OH)_2 + xCa^{2+} \qquad (17)$$

To verify and quantify the cation exchange between Ca^{2+} and Pb^{2+} during adsorption by MPMS, a control experiment was carried out. Under the same experimental conditions, the Ca^{2+} concentration was measured before and after Pb^{2+} addition. The results showed that the Ca^{2+} concentrations of the control without Pb^{2+} and the experiment with 300 mg/L Pb^{2+} were 1.54 mg/L and 19.43 mg/L, respectively. Through calculations using Eq (3-4), the cation exchange between Ca^{2+} and Pb^{2+} was found to contribute 70.96% of the total adsorption, indicating that cation exchange is the main mechanism for the adsorption of Pb^{2+} by MPMS.

4.3. Electrostatic interaction on adsorption of Pb^{2+} by MPMS

When H^+ is present in the solution, HAP and Fe_3O_4 can interact with H^+ as follows [3, 45]:

$$\equiv PO^{-} + H^{+} \leftrightarrow POH \tag{18}$$

$$\equiv CaOH_2^{+} \leftrightarrow CaOH + H^{+} \tag{19}$$

$$\equiv FeOH + H^{+} \leftrightarrow FeOH_2^{+} \tag{20}$$

$$\equiv FeOH \leftrightarrow FeO^{-} + H^{+} \tag{21}$$

When the pH is between 1 and 7, Pb^{2+}, $Pb(OH)^{+}$, and $Pb(OH)_2$ are the main forms of Pb in the solution, and equilibrium can be established at different pH values. At pH ≤ 5, Pb in the solution mainly exists as Pb^{2+}, which can be adsorbed by cation exchange, as discussed above. At pH > 5, Pb^{2+} begins to be converted to $Pb(OH)^{+}$. At pH > 5.5, the Pb in the solution gradually converts to $Pb(OH)_2$ precipitates. For MPMS, when pH < 5, the surface is mainly positively charged owing to $\equiv CaOH_2^{+}$ and $FeOH^{2+}$, which can reduce the adsorption of Pb^{2+} through electrostatic repulsion. At pH > 5, the positive charges of $\equiv CaOH_2^{+}$ and $FeOH^{2+}$ were reduced because of the new equilibrium with a more neutral ≡POH. Hence, as the electrostatic repulsion decreased, the adsorption capacity of MPMS to Pb^{2+} gradually increases.

Furthermore, when a large number of electrostatically repulsive cations are present in the solution, the electrostatic interaction is suppressed. Based on this theory, from the results of Na^{+} in the interfering ion experiment, it can be calculated that the ratio of electrostatic interactions in the MPMS adsorption of Pb^{2+} is only 4.39%.

4.4. Dissolution/Precipitation on adsorption of Pb^{2+} by MPMS

In the control experiment, 1.54 mg/L of Ca^{2+} was leached into the solution. Thus, it can be inferred that HAP can release Ca^{2+} and PO_4^{3-} into the solution through ionization [46]. Leached PO_4^{3-} can form $Pb_3(PO_4)_2$ precipitates with Pb^{2+} in the solution, reducing the Pb^{2+} concentration [47]. However, no obvious $Pb_3(PO_4)_2$ diffraction peaks were detected. Therefore, the dissolution/precipitation mechanism is not feasible for Pb^{2+} adsorption. After calculating the cation exchange, the dissolution/precipitation mechanism only contributed approximately 6.10% of the total Pb^{2+} removal by MPMS.

4.5. Surface complexation on adsorption of Pb^{2+} by MPMS

Recent studies have shown that cations can undergo surface complexation reactions with the hydroxyl groups of adsorbents [45, 48]. The surfaces of Fe_3O_4, HAP, and MS in MPMS can provide complex sites to combine with Pb^{2+}. From the experimental results, the adsorption capacity of MS without MP for Pb^{2+} was 36.66 mg/g. According to the ratio of MS in MPMS, the contribution of MS complexation to the adsorption was only 5.62%. Combined with the surplus contribution rate of 18.55% from the other mechanisms, the contribution of MP complexation to adsorption was approximately 13.17%.

5. Conclusion

This study developed a novel method to improve the separation performance of magnetic materials. By comparing the magnetic separation performance of MP before and after MS loading, it was found that the magnetic separation performance of MP was enhanced after loading onto MS, although the loading reduced the magnetic moment of the MP.

In addition, it was also found that MS loading has little impact on the physicochemical properties of MP. The loaded magnetic sponge MPMS still exhibited a favorable adsorption performance for Pb^{2+}, with cation exchange as the main adsorption mechanism. Loading nanoscale magnetic adsorbents to a three-dimensional structure may become a new direction for magnetic materials. The novel method proposed in this study provides a feasible and cost-effective solution to enhance the downstream separation of magnetic adsorbents for reuse.

Acknowledgements

This study was funded by the Sichuan Science and Technology Program (2019YJ0514). The authors gratefully acknowledge Shiyanjia Lab (www.shiyanjia.com), the editors for handling this article, and the constructive reviews of anonymous reviewers.

Reference

[1] X. Zhan, L. Xiao, B. Liang, Removal of Pb(II) from Acid Mine Drainage with Bentonite-Steel Slag Composite Particles, Sustainability, 11 (2019) 4476.

[2] L.S. Vélez-Pérez, J. Ramirez-Nava, G. Hernández-Flores, O. Talavera-Mendoza, C. Escamilla-Alvarado, H.M. Poggi-Varaldo, O. Solorza-Feria, J.A. López-Díaz, Industrial acid mine drainage and municipal wastewater co-treatment by dual-chamber microbial fuel cells, International Journal of Hydrogen Energy, 45 (2020) 13757-13766.

[3] Y. Bagbi, A. Sarswat, D. Mohan, A. Pandey, P.R. Solanki, Lead (Pb^{2+}) adsorption by monodispersed magnetite nanoparticles: Surface analysis and effects of solution chemistry, J Environ Chem Eng, 4 (2016) 4237-4247.

[4] M. Li, D. Wei, T. Liu, Y. Liu, L. Yan, Q. Wei, B. Du, W. Xu, EDTA functionalized magnetic biochar for Pb(II) removal: Adsorption performance, mechanism and SVM model prediction, Separation and Purification Technology, 227 (2019).

[5] S. Yu, H. Pang, S. Huang, H. Tang, S. Wang, M. Qiu, Z. Chen, H. Yang, G. Song, D. Fu, B. Hu, X. Wang, Recent advances in metal-organic framework membranes for water treatment: A review, Sci Total Environ, 800 (2021) 149662.

[6] S. Zhang, J. Wang, Y. Zhang, J. Ma, L. Huang, S. Yu, L. Chen, G. Song, M. Qiu, X. Wang, Applications of water-stable metal-organic frameworks in the removal of water pollutants: A review, Environ Pollut, 291 (2021) 118076.

[7] B. Wu, J. Ifthikar, D.T. Oyekunle, A. Jawad, Z. Chen, Z. Chen, L. Sellaoui, M. Bouzid, Interpret the elimination behaviors of lead and vanadium from the water by employing functionalized biochars in diverse environmental conditions, Sci Total Environ, 789 (2021) 148031.

[8] X. Zhang, Y. Li, Y. Hou, Preparation of magnetic polyethylenimine lignin and its adsorption of Pb(II), Int J Biol Macromol, 141 (2019) 1102-1110.

[9] S. Shi, Q. Dong, Y. Wang, X. Zhang, S. Zhu, Y.T. Chow, X. Wang, L. Zhu, G. Zhang, D. Xu, Self-supporting super hydrophilic $MgFe_2O_4$ flexible fibers for Pb(II) adsorption, Separation and Purification Technology, 266 (2021).

[10] B. Abraime, K. El Maalam, L. Fkhar, A. Mahmoud, F. Boschini, M. Ait Tamerd, A. Benyoussef, M. Hamedoun, E.K. Hlil, M. Ait Ali, A. El Kenz, O. Mounkachi, Influence of synthesis methods with low annealing temperature on the structural and magnetic properties of $CoFe_2O_4$ nanopowders for permanent magnet application, Journal of Magnetism and Magnetic Materials, 500 (2020) 166416.

[11] A.M. Mudarra Navarro, C.E. Rodríguez Torres, L. Errico, K. Nomura, The role of impurities and oxygen vacancies in the magnetic response of Fe Co Sn_1--O_2. Experimental and ab initio study, Materials Chemistry and Physics, 257 (2021) 123822.

[12] Á. Ríos, M. Zougagh, Recent advances in magnetic nanomaterials for improving analytical processes, TrAC Trends in Analytical Chemistry, 84 (2016) 72-83.

[13] S.V. Bhandare, R. Kumar, A.V. Anupama, H.K. Choudhary, V.M. Jali, B. Sahoo, Mechanistic insights into the sol-gel synthesis of complex (quaternary) Co–Mn–Zn-spinel ferrites: An annealing dependent study, Ceramics International, 46 (2020) 17400-17415.

[14] Z. Lin, P. Yuan, Y. Yue, Z. Bai, H. Zhu, T. Wang, X. Bao, Selective adsorption of Co(II)/Mn(II) by zeolites from purified terephthalic acid wastewater containing dissolved aromatic organic compounds and metal ions, Science of The Total Environment, 698 (2020) 134287.

[15] M.E. Mahmoud, M.F. Amira, A.A. Zaghloul, G.A.A. Ibrahim, High performance microwave-enforced solid phase extraction of heavy metals from aqueous solutions using magnetic iron oxide nanoparticles-protected-nanosilica, Separation and Purification Technology, 163 (2016) 169-172.

[16] Z. Lei, J. Feng, Y. Yang, J. Shen, W. Zhang, C. Wang, An efficient polymer coating for highly acid-stable zeolitic imidazolate frameworks based composite sponges, J Hazard Mater, 382 (2020) 121057.

[17] D. Akın Sahbaz, A. Yakar, U. Gündüz, Magnetic Fe3O4-chitosan micro- and nanoparticles for wastewater treatment, Particulate Science and Technology, 37 (2018) 732-740.

[18] A. Milicevic, S. Belosevic, N. Crnomarkovic, I. Tomanovic, A. Stojanovic, D. Tucakovic, L. Deng, D.F. Che, Numerical study of co-firing lignite and agricultural biomass in utility boiler under variable operation conditions, Int J Heat Mass Tran, 181 (2021).

[19] P. Shi, Y. Wang, X. Hu, M. Duan, X. Wang, Recycle of oil waste via hydrophobic sponge prepared from toner waste, J Hazard Mater, 360 (2018) 615-622.

[20] C. Bai, L. Wang, Z. Zhu, Adsorption of Cr(III) and Pb(II) by graphene oxide/alginate hydrogel membrane: Characterization, adsorption kinetics, isotherm and thermodynamics studies, International Journal of Biological Macromolecules, 147 (2020) 898-910.

[21] M.A. Ahsan, V. Jabbari, M.T. Islam, R.S. Turley, N. Dominguez, H. Kim, E. Castro, J.A. Hernandez-Viezcas, M.L. Curry, J. Lopez, J.L. Gardea-Torresdey, J.C. Noveron, Sustainable synthesis and remarkable adsorption capacity of MOF/graphene oxide and MOF/CNT based hybrid nanocomposites for the removal of Bisphenol A from water, Sci Total Environ, 673 (2019) 306-317.

[22] D.N. Thanh, P. Novák, J. Vejpravova, H.N. Vu, J. Lederer, T. Munshi, Removal of copper and nickel from water using nanocomposite of magnetic hydroxyapatite nanorods, Journal of Magnetism and Magnetic Materials, 456 (2018) 451-460.

[23] H.N. Tran, S.J. You, A. Hosseini-Bandegharaei, H.P. Chao, Mistakes and inconsistencies regarding adsorption of contaminants from aqueous solutions: A critical review, Water Res, 120 (2017) 88-116.

[24] M.A. Ahsan, V. Jabbari, M.A. Imam, E. Castro, H. Kim, M.L. Curry, D.J. Valles-Rosales, J.C. Noveron, Nanoscale nickel metal organic framework decorated over graphene oxide and carbon nanotubes for water remediation, Sci Total Environ, 698 (2020) 134214.

[25] A. Khatoon, M.K. Uddin, R.A.K. Rao, Adsorptive remediation of Pb(II) from aqueous media using Schleichera oleosa bark, Environmental Technology & Innovation, 11 (2018) 1-14.

[26] M. Zhang, G. Lan, H. Qiu, T. Zhang, W. Li, X. Hu, Preparation of ion exchange resin using soluble starch and acrylamide by graft polymerization and hydrolysis, Environ Sci Pollut Res Int, 26 (2019) 3803-3813.

[27] I. Vergili, G. Soltobaeva, Y. Kaya, Z.B. Gönder, S. Çavuş, G. Gürdağ, Study of the Removal of Pb(II) Using a Weak Acidic Cation Resin: Kinetics, Thermodynamics, Equilibrium, and Breakthrough Curves, Industrial & Engineering Chemistry Research, 52 (2013) 9227-9238.

[28] M.T. Islam, R. Saenz-Arana, C. Hernandez, T. Guinto, M.A. Ahsan, H. Kim, Y. Lin, B. Alvarado-Tenorio, J.C. Noveron, Adsorption of methylene blue and tetracycline onto biomass-based material prepared by sulfuric acid reflux, RSC Advances, 8 (2018) 32545-32557.

[29] S. Haq, W. Rehman, M. Waseem, M.-u. Rehman, K.H. Shah, Modeling, Thermodynamic Study and Sorption Mechanism of Cadmium Ions onto Isopropyl Alcohol Mediated Tin Dioxide Nanoparticles, Journal of Inorganic and Organometallic Polymers and Materials, 30 (2019) 1197-1205.

[30] S. Fan, Z. Huang, Y. Zhang, H. Hu, X. Liang, S. Gong, J. Zhou, R. Tu, Magnetic chitosan-hydroxyapatite composite microspheres: Preparation, characterization, and application for the adsorption of phenolic substances,

Bioresour Technol, 274 (2019) 48-55.

[31] J. Couble, D. Bianchi, Experimental microkinetic approach of the CO/H_2 reaction on Pt/Al_2O_3 using the Temkin formalism. 2. Coverages of the adsorbed CO and hydrogen species during the reaction and rate of the CH_4 production, Journal of Catalysis, 352 (2017) 686-698.

[32] Z. Roy, A.V. Palodkar, G. Halder, Biosorptive efficacy of granular activated carbon in pressure swing adsorption based model cooling system: performance assessment, isotherm modeling and cost evaluation, Environ Sci Pollut Res Int, (2021).

[33] S. Masson, C. Vaulot, L. Reinert, S. Guittonneau, R. Gadiou, L. Duclaux, Thermodynamic study of seven micropollutants adsorption onto an activated carbon cloth: Van't Hoff method, calorimetry, and COSMO-RS simulations, Environ Sci Pollut Res Int, 24 (2017) 10005-10017.

[34] J.K. Grewal, M. Kaur, Effect of core-shell reversal on the structural, magnetic and adsorptive properties of Fe_2O_3-GO nanocomposites, Ceramics International, 43 (2017) 16611-16621.

[35] Q.U. Ain, H. Zhang, M. Yaseen, U. Rasheed, K. Liu, S. Subhan, Z. Tong, Facile fabrication of hydroxyapatite-magnetite-bentonite composite for efficient adsorption of Pb(II), Cd(II), and crystal violet from aqueous solution, Journal of Cleaner Production, 247 (2020) 119088.

[36] C.-H. Deng, J.-L. Gong, P. Zhang, G.-M. Zeng, B. Song, H.-Y. Liu, Preparation of melamine sponge decorated with silver nanoparticles-modified graphene for water disinfection, Journal of Colloid and Interface Science, 488 (2017) 26-38.

[37] E.O. López, A.L. Rossi, P.L. Bernardo, R.O. Freitas, A. Mello, A.M. Rossi, Multiscale connections between morphology and chemistry in crystalline, zinc-substituted hydroxyapatite nanofilms designed for biomedical applications, Ceramics International, 45 (2019) 793-804.

[38] Y. Liu, X. Wang, S. Feng, Nonflammable and Magnetic Sponge Decorated with Polydimethylsiloxane Brush for Multitasking and Highly Efficient Oil–Water Separation, Advanced Functional Materials, 29 (2019) 1902488.

[39] O. Kazak, A. Tor, In situ preparation of magnetic hydrochar by co-hydrothermal treatment of waste vinasse with red mud and its adsorption property for Pb(II) in aqueous solution, Journal of Hazardous Materials, 393 (2020) 122391.

[40] H. Gao, P. Sun, Y. Zhang, X. Zeng, D. Wang, Y. Zhang, W. Wang, J. Wu, A two-step hydrophobic fabrication of melamine sponge for oil absorption and oil/water separation, Surface and Coatings Technology, 339 (2018) 147-154.

[41] J. Xiao, R. Hu, G. Chen, Micro-nano-engineered nitrogenous bone biochar developed with a ball-milling technique for high-efficiency removal of aquatic Cd(II), Cu(II) and Pb(II), J Hazard Mater, 387 (2020) 121980.

[42] T. Zhang, J. Chen, H. Xiong, Z. Yuan, Y. Zhu, B. Hu, Constructing new Fe_3O_4@MnO_x with 3D hollow structure for efficient recovery of uranium from simulated seawater, Chemosphere, 283 (2021) 131241.

[43] Y. Zhu, B. Huang, Z. Zhu, H. Liu, Y. Huang, X. Zhao, M. Liang, Characterization, dissolution and solubility of the hydroxypyromorphite-hydroxyapatite solid solution [$(Pb_xCa_{1-x})_5(PO_4)_3OH$] at 25 degrees C and pH 2-9, Geochem Trans, 17 (2016) 2.

[44] C. Nataraj, S. Khan, M.H. Habaebi, Coil geometry models for power loss analysis and hybrid inductive link for wireless power transfer applications, Sādhanā, 43 (2018).

[45] I. Smiciklas, I. Dimovic, M. Mitric, Removal of Co^{2+} from aqueous solutions by hydroxyapatite, Water Res, 40 (2006) 2267-2274.

[46] L. Dong, S. Zhu, M. Xia, Y. Chu, F. Wang, W. Lei, Molecular dynamics simulations of the binging affinity of 1-hydroxyethane-1, 1-diphosphonic acid (HEDP) with nano-hydroxyapatite and the uptake of Cu(2+) by HEDP-HAP hybrid systems, J Hazard Mater, 383 (2020) 121206.

[47] F. Gode, E. Pehlivan, Removal of chromium(III) from aqueous solutions using Lewatit S 100: the effect of pH, time, metal concentration and temperature, J Hazard Mater, 136 (2006) 330-337.

[48] A. Uheida, G. Salazar-Alvarez, E. Bjorkman, Z. Yu, M. Muhammed, Fe_3O_4 and gamma-Fe_2O_3 nanoparticles for the adsorption of Co^{2+} from aqueous solution, J Colloid Interface Sci, 298 (2006) 501-507.